Multi-Objective Petrophysical Seismic Inversion Based on the Double-Porosity Biot–Rayleigh Model

Qiang Guo[1,2] · Jing Ba[2] · José M. Carcione[2,3]

Abstract

Petrophysical seismic inversion, aided by rock physics, aims at estimating reservoir properties based on reflection events, but it is generally based on the Gassmann equation, which precludes its applicability to complex reservoirs. To overcome this problem, we present a methodology based on the double-porosity Biot–Rayleigh (BR) model, which takes into account the rock heterogeneities. The volume ratio of inclusions in the BR model is treated as a spatially varying parameter, facilitating a better description of the pore microstructure. The method includes the Zoeppritz equations to extract reservoir properties from prestack data. To handle the ill-posedness of the inversion and achieve a stable solution, the algorithm is formulated as a multi-objective optimization based on the Bayes theorem, where the reservoir-property estimation is jointly conditioned to seismic and elastic data with multiple prior terms. The method is validated with field data of a tight gas sandstone reservoir, illustrating its effectiveness compared to the Gassmann-based estimation, reducing uncertainties and improving the accuracy of identifying gas zones.

Article Highlights

- The petrophysical seismic inversion is based on the double-porosity Biot–Rayleigh model
- Spatially varying inclusion volumes are used to describe complex pore structures
- A multi-objective optimization with joint data misfit enables stable results

---

✉ Jing Ba
  jba@hhu.edu.cn

1   College of Information Engineering, China Jiliang University, 310018 Hangzhou, China

2   School of Earth Sciences and Engineering, Hohai University, 211100 Nanjing, China

3   National Institute of Oceanography and Applied Geophysics (OGS), 34010 Trieste, Italy

1 Introduction

Seismic inversion aided by rock physics (so-called petrophysical seismic inversion) estimates reservoir properties from reflection data (Gunning and Glinsky 2007; Bosch et al. 2010; Zong et al. 2015; Grana et al. 2017; Luo et al. 2020; Huang et al. 2021a). The seismic and petrophysical inversions can be implemented either sequentially or jointly. The sequential method carries out the petrophysical inversion from elastic or impedance models (Hammer et al. 2012; Zhao et al. 2013; Hafez et al. 2014), whereas the joint one performs the two inversions simultaneously (Zong et al. 2015; Aleardi et al. 2018; Fjeldstad et al. 2021). Moreover, the methodology can be deterministic or probabilistic. The first usually linearizes/approximates a rock-physics model or a seismic reflectivity and an analytic solution to the inverse problem can be derived (Hansen et al. 2006; Huang et al. 2021b). The probabilistic approach formulates an objective function (or posterior probability) based on the Bayes theorem and nonlinear seismic and petrophysical forward operators (Bachrach 2006; Spikes et al. 2007). In practice, an inverse problem can be solved either by a stochastic sampling (Mosegaard 1998; Bosch et al. 2007) or a global optimization algorithm (Sambridge and Mosegaard 2002; Sen and Stoffa 2013). In general, the joint approach can avoid accumulative errors that might be present in the sequential one, and the probabilistic approach can handle nonlinear rock-physics and seismic models, assessing the uncertainties of the results. Moreover, the adopted rock-physics model can be empirical or theoretical. The former requires a fit with experimental data (Avseth and Veggeland 2014; Aleardi et al. 2018) or spatial mapping relations assisted by geostatistical stochastic modeling (González et al. 2008; Connolly and Hughes 2016; Azevedo et al. 2019), while the theoretical approach is based on predictive models (Zhao et al. 2013; Teillet et al. 2021; Li et al. 2021), which is more adapted to specific or complex geological/lithological conditions.

Many rock-physics models have been proposed as, for instance, effective medium theories (Mavko et al. 2009), which involve inclusion models (Norris 1985; Markov et al. 2005) and contact models (Avseth and Bachrach 2005; Dvorkin et al. 2014). The Gassmann equation (Gassmann 1951) is the zero-frequency limit of the dynamic poroelasticity theory and provides an approximation of the seismic velocity, and mineral heterogeneity can be handled with averaging (e.g., Xu and White 1995). These models assume homogeneous properties at the seismic scale, which facilitates the inversion for conventional reservoirs (e.g., Zong et al. 2015; Grana, 2020; Teillet et al. 2021; Bredesen et al. 2021; Guo et al. 2021a), but fail when dealing with reservoirs, where complex pore microstructures and fluid patches are present. To overcome this problem, much work has been done by considering meso- and micro-scale heterogeneities, including attenuation/ dispersion effects (Dvorkin and Nur 1993; Santos et al. 2004; Pride et al. 2004; Ba et al. 2011, 2017; Wang and Tang 2021; David and Zimmerman 2012; Gurevich et al. 2009; Carcione et al. 2013). However, such models usually employ sequential approaches and mainly non-iterative inversion methods (Picotti et al. 2018; Pang et al. 2021).

Petrophysical seismic inversion involves two mainly aspects, namely to improve the accuracy/applicability of the forward modeling, e.g., modeling the rock skeleton by considering multiple pore shapes/types (Guo et al. 2021b; Wang et al. 2021), or deriving a reflectivity formula based on sensitive geofluid/petrophysical parameters (Pan and Zhang 2018; Chen et al. 2021). A third aspect is to mitigate the instability/non-uniqueness of the inversion process, e.g., by incorporating reliable/multiple prior information into the objective function (Grana 2020; Astic et al. 2021), or designing advanced optimization/sampling algorithms (de Figueiredo et al. 2019; Zidan et al. 2021). Although these methods improve or stabilize the results

to some extent, they are based on homogeneous models (hereafter referred to as the Gassmann model) and cannot be appropriate for complex reservoirs. On the other hand, using heterogeneous models has two main drawbacks. First, the integrated petro-seismic forward operator can be highly nonlinear and the petrophysical parameters may have a low sensitivity to the seismic response, thus causing instabilities. Second, the heterogeneous model usually requires more parameters (e.g., crack density and pore aspect ratio), which also contributes to the instabilities.

We present a methodology based on a heterogeneous rock-physics theory, namely the Biot–Rayleigh (BR) model (Ba et al. 2011). By incorporating the predicted elastic parameters into the Zoeppritz equation (Aki and Richards 1980), we extract the reservoir properties from seismic-angle gathers. In practice, we assign a volume fraction of inclusions in the BR equation as a spatially varying parameter (in addition to porosity and fluid saturation), by which a complex pore structure can be modeled as a double-porosity medium. Moreover, to stabilize the algorithm, we formulate it as a multi-objective optimization problem based on the Bayes theorem. The estimation of the parameters is jointly conditioned by the seismic and petro-elastic data, based on multiple prior terms from a Gaussian mixture model. The problem is treated as a weighted objective function, minimized by a simulated annealing algorithm to achieve a stable solution. The methodology is applied to field data acquired from a tight gas sandstone reservoir in the Sichuan Basin, China, and compared to the Gassmann model.

2 Theory and Method

2.1 Forward model relating the seismic responses to petrophysical properties

In order to model the complexity of reservoirs, we employ the BR model (Ba et al. 2011) to describe the seismic wave propagation. This model assumes a double-porosity medium, where spherical inclusions are embedded into a host medium with two pore structures (the governing equations are given in Appendix A). Differing from the Gassmann model, the BR model considers heterogeneities that may be caused by fluid distribution, mineral grains and pore structures.

The forward modeling consists in three steps, i.e., estimating first the properties of the mineral mixture, then those of the skeleton, and finally those of the wet rock. For simplicity, we express the mapping of the petrophysical parameters $\mathbf{r}$ to the elastic parameters $\mathbf{m}$, based on the BR equation, as

$$\mathbf{m} = \mathbf{R}(\mathbf{r}, \mathbf{L}), \tag{1}$$

where $\mathbf{R}$ is the forward operator, $\mathbf{m}$ includes the P- and S-wave velocities and bulk density, $\mathbf{r}$ involves parameters such as the total porosity and fluid saturation, and $\mathbf{L}$ denotes an auxiliary parameter.

To extract petrophysical parameters directly from seismic data, we combine rock-physics modeling and prestack amplitude variation with offset (AVO) inversion, i.e., the predicted elastic parameters are incorporated into the Zoeppritz equation (Aki and Richards 1980), based on which we obtain the forward model that relates the petrophysical parameters to the seismic response. We express the integrated forward model as

$$\mathbf{d}_{\text{seis}} = \mathbf{G}(\mathbf{R}(\mathbf{r}, \mathbf{L})) * \mathbf{w} + \mathbf{e}, \tag{2}$$

where **G** is the Zoeppritz equation, **w** is the source wavelet (the symbol "*" denotes time convolution), $\mathbf{d}_{\text{seis}}$ is the PP-wave prestack seismic data, and **e** is random error caused by the modeling or measurements. Since the forward operators **R** and **G** are nonlinear, the integrated forward model may exhibit a high nonlinearity, and the inverse problem can be unstable.

The BR model assumes that stiff and soft pores (e.g., cracks) are randomly distributed spatially; hence, the rock skeleton exhibits the isotropic properties as a whole. Besides, the double-porosity model can be treated as a homogeneous media at the seismic scale (~ 50 Hz) since the inclusions have a radius of ~ 0.05 m (which is much smaller than the seismic wavelength). Therefore, the Zoeppritz equation which is under the isotropic and homogeneous assumption can be combined with the BR model at seismic frequencies.

2.2 Multi-objective petrophysical seismic inversion

To evaluate the uncertainty of the result, we cast the inverse problem into the Bayes theorem, where the posterior distribution of the model parameters **z** given the observation **d** can be expressed as (Buland and Omre 2003)

$$P(\mathbf{z}|\mathbf{d}) = \frac{P(\mathbf{d}|\mathbf{z}) \times P(\mathbf{z})}{P(\mathbf{d})} \propto P(\mathbf{d}|\mathbf{z}) \times P(\mathbf{z}), \tag{3}$$

where $P(\mathbf{d}|\mathbf{z})$ is the likelihood function that describes the relation between **z** and **d** and $P(\mathbf{d})$ is the marginal probability of **d** that can be viewed as a constant. To jointly estimate the petrophysical and auxiliary parameters, we set $\mathbf{z} = [\mathbf{r}, \mathbf{L}]^{\text{T}}$, where the choice of **L** will be discussed later.

The seismic response to petrophysical parameters based on the BR model is highly nonlinear, and it is difficult to estimate the model parameters only from seismic data. To this end, we enable the estimation to be jointly conditioned to seismic and elastic data. By treating these ($\mathbf{d}_{\text{seis}}$ and $\mathbf{d}_{\text{elas}}$) as the observation, we express Eq. (3) as

$$P(\mathbf{z}|\mathbf{d}_{\text{seis}}, \mathbf{d}_{\text{elas}}) \propto P(\mathbf{d}_{\text{seis}}, \mathbf{d}_{\text{elas}}|\mathbf{z}) \times P(\mathbf{z}). \tag{4}$$

By considering that $P(\mathbf{d}_{\text{seis}}, \mathbf{d}_{\text{elas}}|\mathbf{z}) = P(\mathbf{d}_{\text{seis}}|\mathbf{z},\mathbf{d}_{\text{elas}}) \times P(\mathbf{d}_{\text{elas}}|\mathbf{z})$, and assuming $P(\mathbf{d}_{\text{seis}}|\mathbf{z},\mathbf{d}_{\text{elas}}) \approx P(\mathbf{d}_{\text{seis}}|\mathbf{z})$, we rewrite Eq. (4) as

$$P(\mathbf{z}|\mathbf{d}_{\text{seis}}, \mathbf{d}_{\text{elas}}) \propto P(\mathbf{d}_{\text{seis}}|\mathbf{z}) \times P(\mathbf{d}_{\text{elas}}|\mathbf{z}) \times P(\mathbf{z}). \tag{5}$$

Because the statistical characteristics of **z** usually vary in different lithofacies under complex geological conditions, the Gaussian mixture model (Sauvageau et al. 2014; Grana et al. 2017) is employed to describe its prior distribution. As a linear combination of Gaussian distributions, it takes the form

$$P(\mathbf{z}) = \sum_{k=1}^{N_c} \pi_k \text{N}_k(\mathbf{z}; \boldsymbol{\mu}_{\mathbf{z}|k}, \boldsymbol{\Sigma}_{\mathbf{z}|k}), \tag{6}$$

where N_k denotes the kth Gaussian component with mean $\boldsymbol{\mu}_{\mathbf{z}|k}$ and covariance matrix $\boldsymbol{\Sigma}_{\mathbf{z}|k}$, π_k is the weight of the linear combination that satisfies $\Sigma_{k=1}^{N_c} \pi_k = 1$, and N_c is the number of components.

We assume that the error in Eq. (2) follows a zero-mean Gaussian distribution. By substituting Eqs. (1), (2), (6) into (5), the posterior distribution becomes a linear combination of posterior components $P_k(\mathbf{z}|\mathbf{d}_{\text{seis}},\mathbf{d}_{\text{elas}})$ ($k = 1,2,\ldots,N_c$) as

$$P(\mathbf{z}|\mathbf{d}_{\text{seis}},\mathbf{d}_{\text{elas}}) = \sum_{k=1}^{N_c} \pi_k P_k(\mathbf{z}|\mathbf{d}_{\text{seis}},\mathbf{d}_{\text{elas}}), \tag{7}$$

with

$$P_k(\mathbf{z}|\mathbf{d}_{\text{seis}},\mathbf{d}_{\text{elas}}) = C_k \exp\left[-\frac{1}{2\sigma_{\text{s}}}\|\mathbf{d}_{\text{seis}} - \mathbf{G}(\mathbf{R}(\mathbf{z}))\|_2 - \frac{1}{2\sigma_{\text{e}}}\|\mathbf{d}_{\text{elas}} - \mathbf{R}(\mathbf{z})\|_2 \right.$$
$$\left. -\frac{1}{2}\left(\mathbf{z} - \boldsymbol{\mu}_{\mathbf{z}|k}\right)^{\mathrm{T}}\left(\boldsymbol{\Sigma}_{\mathbf{z}|k}\right)^{-1}\left(\mathbf{z} - \boldsymbol{\mu}_{\mathbf{z}|k}\right)\right], \tag{8}$$

where C is a normalization constant and σ_{s} and σ_{e} are the data variances associated with the seismic and elastic observations, respectively.

The estimation of $\mathbf{z}$ can be achieved by maximizing all the posterior objective components in Eq. (8), which can be treated as a multi-objective optimization problem. Each component can be expressed as the negative logarithmic form of P_k. Then, we solve the problem by minimizing a linear combination of the components weighted by π_k, which leads to the following objective function

$$F_{\text{obj}}(\mathbf{z}) = \sum_{k=1}^{N_c} \pi_k\left[\frac{1}{2\sigma_{\text{s}}}\|\mathbf{d}_{\text{seis}} - \mathbf{G}(\mathbf{R}(\mathbf{z}))\|_2 + \frac{1}{2\sigma_{\text{e}}}\|\mathbf{d}_{\text{elas}} - \mathbf{R}(\mathbf{z})\|_2 \right.$$
$$\left. +\frac{1}{2}\left(\mathbf{z} - \boldsymbol{\mu}_{\mathbf{z}|k}\right)^{\mathrm{T}}\left(\boldsymbol{\Sigma}_{\mathbf{z}|k}\right)^{-1}\left(\mathbf{z} - \boldsymbol{\mu}_{\mathbf{z}|k}\right)\right]. \tag{9}$$

The weights of the objective components should be carefully selected to achieve a stable and accurate result.

2.3 Multi-objective optimization approach

Without loss of generality, we assume that the rock contain two primary lithofacies, classified as reservoir and non-reservoir rocks. Therefore, for two Gaussian components ($N_c = 2$), the objective function can be rewritten as

$$F_{\text{obj}}(\mathbf{z}) = \frac{\pi_1 + \pi_2}{\sigma_{\text{s}}}\|\mathbf{d}_{\text{seis}} - \mathbf{G}(\mathbf{R}(\mathbf{z}))\|_2 + \frac{\pi_1 + \pi_2}{\sigma_{\text{e}}}\|\mathbf{d}_{\text{elas}} - \mathbf{R}(\mathbf{z})\|_2 + \pi_1\Omega_1 + \pi_2\Omega_2, \tag{10}$$

with

$$\Omega_k = \left(\mathbf{z} - \boldsymbol{\mu}_{\mathbf{z}|k}\right)^{\mathrm{T}}\left(\boldsymbol{\Sigma}_{\mathbf{z}|k}\right)^{-1}\left(\mathbf{z} - \boldsymbol{\mu}_{\mathbf{z}|k}\right), \; k = 1, 2. \tag{11}$$

By introducing posterior weights $\boldsymbol{\beta}$ (to replace the objective component weights and data variances) and considering $\pi_1 + \pi_2 = 1$, Eq. (10) can be further expressed as

$$F_{\text{obj}}(\mathbf{z}) = \|\mathbf{d}_{\text{seis}} - \mathbf{G}(\mathbf{R}(\mathbf{z}))\|_2 + \beta_1\|\mathbf{d}_{\text{elas}} - \mathbf{R}(\mathbf{z})\|_2 + \beta_2\left[\pi_1(\Omega_1 - \Omega_2) + \Omega_2\right], \tag{12}$$

where the posterior weights $\boldsymbol{\beta} = [\beta_1, \beta_2]^T$ aim at balancing the two data misfits and the prior terms during the optimization process.

We use a fast simulated annealing (FSA) algorithm (Ingber and Rosen 1992; Sen and Stoffa 2013) to optimize the objective function of Eq. (12). Besides, we iteratively update the posterior weights by the maximum likelihood method during the FSA-based optimization process.

In practice, the model perturbation and the acceptance probability at the $(n+1)$th iteration can be expressed as (Ryden and Park 2006)

$$\mathbf{z}^{(n+1)} = \mathbf{z}^{(n)} + \left(\frac{T^{(n+1)}}{T^{\text{init}}} \eta_1 \tan\left(\eta_2 \frac{\pi}{2} \right) \right) \Delta \mathbf{z}, \tag{13}$$

and

$$P\left(\mathbf{z}^{(n)} \rightarrow \mathbf{z}^{(n+1)} \right) = \min\left[1, \exp\left(-\frac{F_{\text{obj}}\left(\mathbf{z}^{(n+1)} \right) - F_{\text{obj}}\left(\mathbf{z}^{(n)} \right)}{T^{(n+1)}} \right) \right], \tag{14}$$

where η is a random number between 0 and 1 and $T^{(n+1)}$ and T^{init} are the current and initial temperatures, respectively. The perturbation and its acceptance (or rejection) are repeated several times (defined by the Markov chain length). The optimization/sampling proceeds as the temperature anneals until the maximum iteration or the ending temperature is reached.

We update $\boldsymbol{\beta}$ by maximizing the likelihood function $P(\mathbf{d}|\boldsymbol{\beta})$ as

$$\hat{\boldsymbol{\beta}} = \arg \max_{\boldsymbol{\beta}} P\left(\mathbf{d}_{\text{seis}}, \mathbf{d}_{\text{elas}} | \boldsymbol{\beta} \right). \tag{15}$$

By taking the negative logarithmic form of $P(\mathbf{d}|\boldsymbol{\beta})$ as $L(\boldsymbol{\beta})$, the estimation of Eq. (15) can be achieved by minimizing $L(\boldsymbol{\beta})$. Here, we employ the Gauss–Newton method to update $\boldsymbol{\beta}$ iteratively, by which $\boldsymbol{\beta}$ at the $(n+1)$th iteration is updated by

$$\beta_i^{(n+1)} = \beta_i^{(n)} - \left[\left(\frac{\partial L}{\partial \beta_i} \right)^T \left(\frac{\partial L}{\partial \beta_i} \right) \right] \frac{\partial L}{\partial \beta_i}, \ i = 1, 2. \tag{16}$$

The analytic computation of the derivative of $L(\boldsymbol{\beta})$ is estimated via the expectations of the posterior and prior distributions (Jalobeanu et al. 2002; Guo et al. 2021a). In practice, the model perturbation of the FSA proceeds at inner and outer loops, respectively. In each outer loop (at a fixed temperature), the empirical mean of the Monte Carlo sampling for the model parameters (after completing all inner loops) is used to compute the expectations, the derivative of $L(\boldsymbol{\beta})$ can be achieved, and $\boldsymbol{\beta}$ is updated. Then, the model perturbation continues to the next outer loop (with temperature reduced), and the sampling of model parameters and the update of $\boldsymbol{\beta}$ are repeated. Note that the superscript n in Eq. (16) only denotes the iteration of the outer loop, whereas that in Eqs. (13) and (14) denotes the total iteration. The expression and computation of the derivative in Eq. (16) are given in Appendix B.

2.4 Workflow

For complex reservoirs (e.g., tight gas sandstone reservoirs), the pore structure and mineral components often exhibit inhomogeneous distributions. In the BR model, spherical inclusions with a low volume ratio v_c are embedded in a host medium with a higher
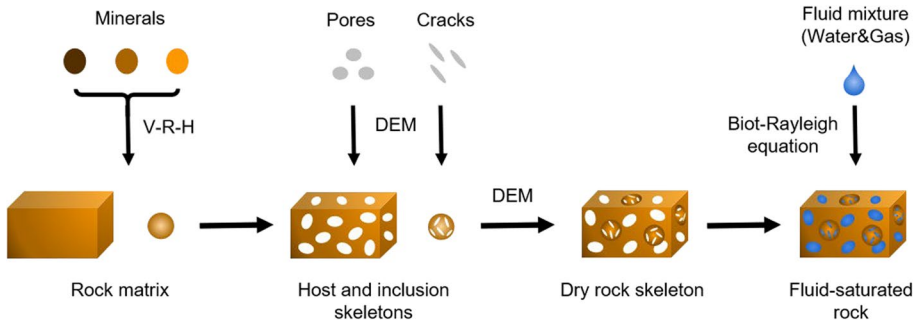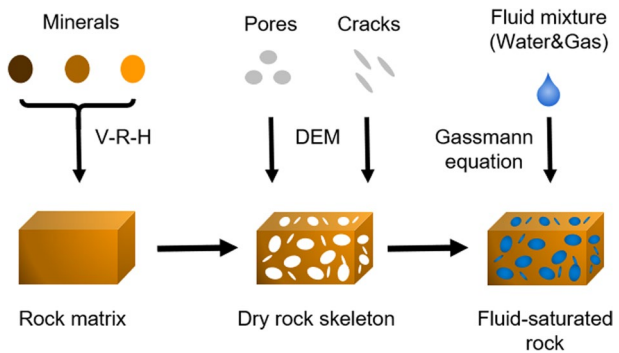
Fig. 1 Workflow of the Biot–Rayleigh-based rock-physics modeling

Fig. 2 Workflow of the DEM-Gassmann-based rock physics modeling

volume ratio v_h. The total rock porosity is $\phi = \phi_{10}v_h + \phi_{20}v_c$ with $v_h + v_c = 1$, where ϕ_{10} and ϕ_{20} are the porosities of the two porous components. To account for the fabric heterogeneities, we treat the volume ratio of inclusions (inclusion volume) v_c as an auxiliary parameter **L**. In practice, we set the inclusion volume as an spatially variable vector $\mathbf{v} = [v_1, v_2, \ldots, v_m]^T$ (with m denoting the sample number at each seismic trace) during the inversion process, which honors the heterogeneity and improves the accuracy of the modeling.

The workflow of the BR rock-physics modeling is shown in Fig. 1. First, the elastic properties of the mineral mixture are computed by the Voigt–Reuss–Hill average. Then, by adding cracks and pores into the inclusion and host media with the differential effective medium (DEM) model (Berryman et al., 2002), the elastic properties of the two skeletons are obtained, and subsequently we add the inclusions into the host medium to compute those of the skeleton. Finally, the wet-rock properties are computed with the BR equation. We perform a plane-wave analysis on the BR differential equations to obtain the phase velocity of the P wave (see Appendix A). The S-wave velocity is computed from the shear modulus of the skeleton and the density of the fluid-saturated rock. The bulk modulus of the fluid mixture (brine and gas) is obtained from the Wood equation.

The Xu–White model (Xu and White 1995) is combined with the Gassmann model and compared with the proposed method. In the Gassmann model, the skeleton moduli are obtained with the DEM method, followed by fluid substitution (see Fig. 2).

The inclusion volume $\mathbf{v}$ cannot be directly obtained from observed data, and we estimate it via well-log calibration by matching the predicted and log P-wave velocities, $\mathbf{V}_P^{est}$ and $\mathbf{V}_P^{log}$, respectively, i.e.,

$$\hat{\mathbf{v}} = \arg\min_{\mathbf{v}} \left\| \mathbf{V}_P^{est}(\mathbf{r}, \mathbf{v}) - \mathbf{V}_P^{log} \right\|_2, \tag{17}$$

Moreover, since the proposed method requires the elastic model as input data in Eq. (12), we obtain this model from a conventional prestack AVO inversion by

$$\hat{\mathbf{m}} = \arg\min_{\mathbf{m}} \left[\frac{1}{2\sigma_s} \left\| \mathbf{d}_{seis} - \mathbf{G}(\mathbf{m}) \right\|_2 + \frac{1}{2} \left(\mathbf{m} - \boldsymbol{\mu}_{\mathbf{m}} \right)^T \left(\boldsymbol{\Sigma}_{\mathbf{m}} \right)^{-1} \left(\mathbf{z} - \boldsymbol{\mu}_{\mathbf{m}} \right) \right], \tag{18}$$

where $\boldsymbol{\mu}_{\mathbf{m}}$ and $\boldsymbol{\Sigma}_{\mathbf{m}}$ are the mean and covariance matrix of the elastic parameters, respectively. For simplicity, we assume the elastic parameters follow a standard Gaussian distribution [in Eq. (18)], whereas the Gaussian mixture model can be used alternatively. We set the P-wave velocity of the BR model as the elastic data $\mathbf{d}_{elas}$ in the objective function of Eq. (12).

In summary, Fig. 3 outlines the workflow of the proposed inversion method as follows:

(1) Initialize the rock-physics parameters, estimating the inclusion volume $\mathbf{v}$ with Eq. (17), and the P-wave velocity model $\mathbf{m}$ with Eq. (18);
(2) The rock-physics modeling is performed to formulate the elastic misfit with the estimated $\mathbf{m}$ and the seismic misfit with the prestack seismic data;
(3) Estimate the Gaussian mixture model of Eq. (6) from the log-measured porosity and water saturation and $\mathbf{v}$ (from Step 1) by using the expectation–maximization algorithm, formulating the prior term, and building the objective function of Eq. (12);

Fig. 3 Workflow of the proposed inversion method
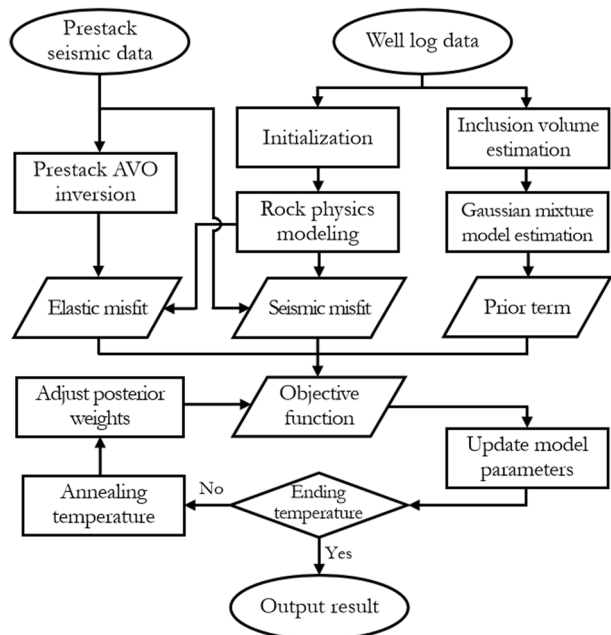
(4) Initialize the parameters of the FSA, i.e., the initial temperature, the temperature damp-
     ing factor, the Markov-chain length (inner loops), and the chain number (outer loops);
(5) Perturb the model parameters according to Eq. (13) with its acceptance/rejection
     according to Eq. (14), and repeat the model update several times defined by the inner
     loops;
(6) Update the posterior weights according to Eq. (16), reducing the temperature, and
     switching to the next chain (outer loop);
(7) Repeat steps 5–6 till the model update is complete for all the chains, and **z** is output as
     the final result.

3 Test and application

The method is tested and applied on field seismic data acquired from a tight gas sand-
stone reservoir in Sichuan Basin, China. The data set includes two well logs and a pre-
stack seismic section. We first build the rock-physics modeling by using the Gassmann and
BR models, extract prior information of petrophysical parameters, followed by inversion/
uncertainty tests based on Well 1, and finally validate the method by inverting the seismic
section with a blind test on Well 2.

3.1 Rock-physics modeling

The reservoir has low porosity and permeability and contains relatively high clay content,
where microcracks are well developed. Figure 4 displays the log curves and the borehole-
side angle gather of Well 1, used for the calibration by using the Gassmann (Fig. 1) and
BR (Fig. 2) models. Table 1 shows the rock-physics parameters for the tests. The BR
equation is evaluated at seismic frequencies (Wang et al. 2020). In this approach, the rock
matrix (for host and inclusions) is a mixture of quartz, clay, and feldspar minerals with
their percentages of 68.4, 15.2, and 16.4%, respectively; the cracks are modeled by the
inclusions, where the inclusion volume (v) quantifies the relative percentage of cracks and
pores with the aspect ratios of 0.035 and 0.12, respectively. Figure 5a and b shows the
predicted P-wave velocity by the two models as a function of porosity and clay/inclusion
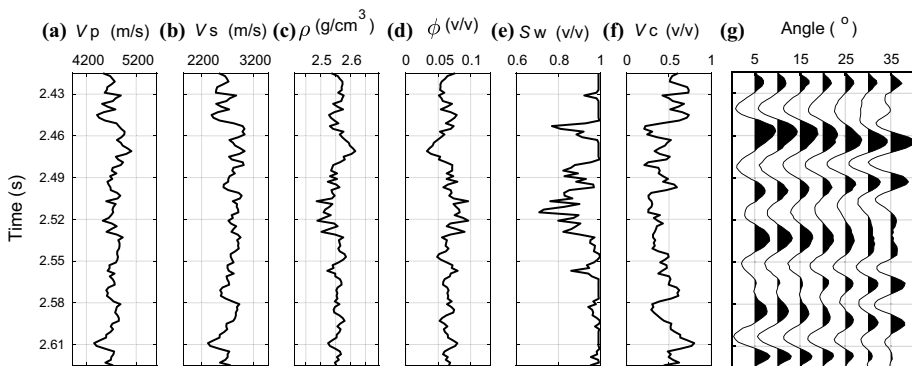

Fig. 4 Well-log data of **a** P-, **b** S-wave velocities, **c** density, **d** total porosity, **e** water saturation, **f** clay vol-
ume, and **g** angle gather

Table 1 Rock properties

Bulk moduli of quartz, K_{qz}	42 GPa
Shear moduli of quartz, μ_{qz}	37 GPa
Density of quartz, ρ_{qz}	2.66 g/cm^3
Bulk moduli of feldspar, K_{ds}	75 GPa
Shear moduli of feldspar, μ_{ds}	26 GPa
Density of quartz, ρ_{ds}	2.72 g/cm^3
Bulk moduli of clay, K_{cl}	23 GPa
Shear moduli of clay, μ_{cl}	7 GPa
Density of clay, ρ_{cl}	2.25 g/cm^3
Bulk moduli of brine, K_w	2.2 GPa
Bulk moduli of gas, K_g	0.0015 GPa
Density of brine, ρ_w	1.1 g/cm^3
Density of gas, ρ_g	0.002 g/cm^3
Aspect ratio of pore, α_s	0.12
Aspect ratio of crack, α_c	0.035
Radius of inclusion, R_o	0.05 m
Permeability of host, κ_1	0.01 D
Viscosity of fluid, η	0.001 Pa·s
Angular frequency, ω	94π rad/s

volume, respectively, where we can see that the BR model exhibits a better agreement for the well samples which have a low clay volume (which are mainly gas-saturated rocks) and for the gas-reservoir samples that have a relatively low water saturation (Fig. 5c), while the Gassmann model generally underestimates the velocity (Fig. 5d).

Figure 6a, b shows the predicted elastic parameters by the Gassmann and BR model that are calibrated on Well 1, respectively. The Gassmann prediction (with fixed aspect ratio) exhibits an apparent deviation in the gas-saturated section (2.49–2.53 s). Although the prediction with spatially varying aspect ratios (Yan et al. 2002; Guo et al. 2021b) improves the agreement to some extent (see Fig. 6d), it requires two extra parameters for the DEM modeling, i.e., the sand- and clay-related pore aspect ratios (Fig. 6e, f). Remarkably, the BR model (Fig. 6b) exhibits the best agreement among the three, and it only requires the inclusion volume [see Fig. 6c, estimated by Eq. (17)] to achieve the desired accuracy. The estimated curves of the aspect ratio (Fig. 6e, f) and the inclusion volume (Fig. 6c) are given. The inclusion volume, which cannot be directly measured, is treated as an auxiliary parameter to describe the spatial complexity of pore structure and facilitate the accuracy of rock physics modeling.

3.2 Well-log data test

The estimated inclusion volume (Fig. 6c) and the log porosity and saturation (Fig. 4d, e) are employed to extract the prior information for the inversion. Figure 7a–c shows the Gaussian mixture distribution of the model parameters (with two Gaussian components weighted by 0.32 and 0.68, estimated by the expectation–maximization algorithm), by which the prior term is formulated. Particularly, the inclusion volume exhibits a fairly good correlation with the clay volume (see Fig. 7d), from which an empirical relationship can be derived. Since the inclusions with microcracks are primarily determined by clay minerals
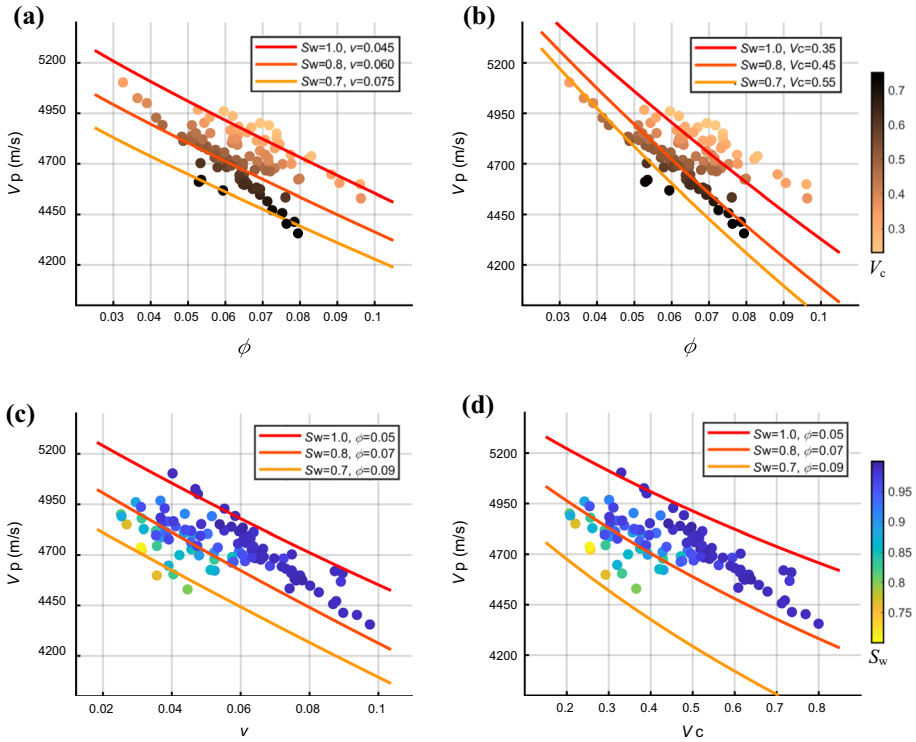
Fig. 5 Predicted P-wave velocity as a function of (**a**, **b**) porosity and (**c/d**) inclusion/clay volume, by using the (**a**, **c**) BR and **b**, **d** Gassmann rock-physics models, overlapped by well-log samples color-coded by **a**, **b** clay volume and **c**, **d** water saturation. The well samples in **c** correspond to the clay volume ranging from 0.15 to 0.85

where soft pores are likely developed (Xu and White 1995), such a correlation is reasonable in tight gas sandstones.

We carry out three inversion tests by using the Gassmann model, and the BR model with single misfit and joint misfits (the proposed method). The last two tests are designed to validate the effectiveness of the multi-objective optimization. For the joint misfits, a low-frequency filtered P-wave velocity (it has a correlation coefficient of 0.85 with the log curve) is used as the input elastic model. The initial temperature and damping factor of the FSA are set to 1.05 and 0.98, respectively. For each simulation, the total iteration is 20000 (with 500 inner loops and 40 outer loops).

Figure 8a–c shows the three test results. In each test, fifty independent simulations are performed, of which the mean result (red) and one simulation result (yellow) are displayed. By comparing the results by using the Gassmann and BR models (Fig. 8a, b), the latter shows the best agreement for all the petrophysical parameters. See Table 2 for a quantitative comparison. The clay volume for the BR method is obtained from the inclusion volume according to the empirical relation shown in Fig. 7d. The BR model with joint misfits, based on the multi-objective optimization, further improves the accuracy (Fig. 8c). Figure 8d displays an overall comparison of the three results, indicating that the proposed method delineates the gas- and water-saturated zones more distinctively aided by the
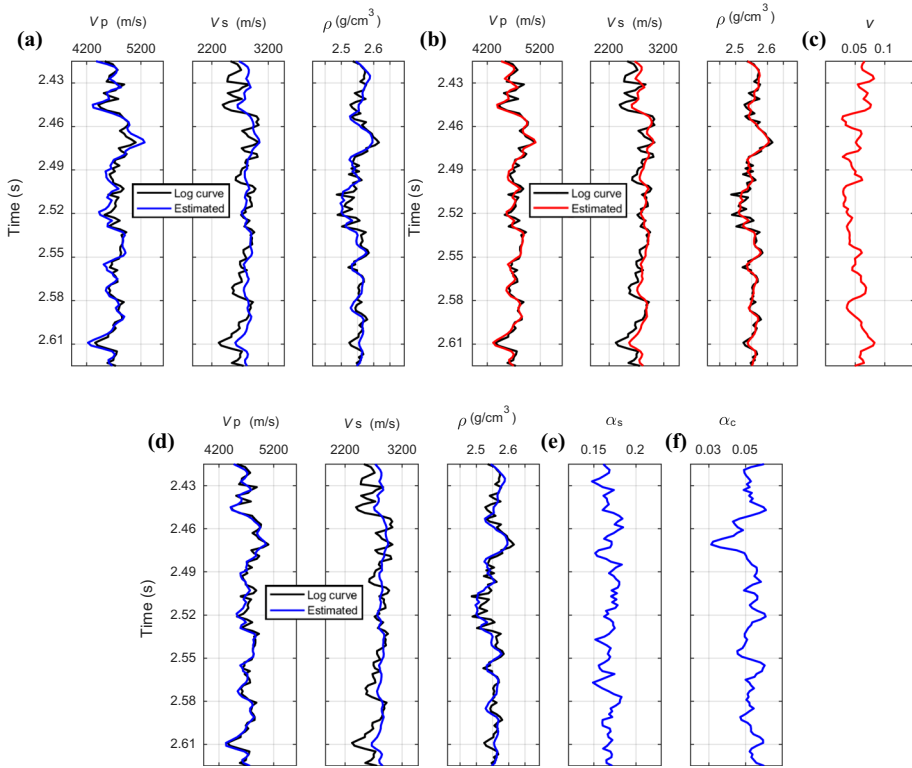
Fig. 6 Predicted elastic parameters by using **a** the Gassmann model with fixed aspect ratio, **b** the BR method with **c** the estimated inclusion volume, and **d** the Gassmann model with the estimated **e** sand-related and **f** clay-related pore aspect ratios. The predictions in **a** and **b** use fixed aspect ratios of $\alpha_s = 0.13$ and $\alpha_c = 0.02$

porosity and clay volume (indicated by the arrows). However, the saturation shows less improvement, considering that the tight gas sandstone is less insensitive to fluid saturation. Figure 9 shows the misfit evolution during the inversion process for the BR model with single and joint misfits, from which we can see that the proposed multi-objective inversion, conditioned to seismic and elastic data, achieve a better convergence on the elastic misfit (Fig. 9a), which improves the convergence of the seismic misfit (Fig. 9b).

The uncertainty analysis is also performed by considering the randomness of the algorithm. Figure 10 shows the posterior probability distributions for the three tests, estimated by setting the objective function with a fixed temperature of 0.25 (which corresponds to 15% data variance. At each spatial/temporal point, the distribution is estimated from one hundred samplings, each sampling runs for a Markov chain length of 10,000 to achieve the stationary state. Comparing the results in Fig. 10a–c, we observe that the BR model generally predicts a narrow distribution tail (Fig. 10c) with fewer uncertainties. The The maximum of the a posteriori (MAP) results (red curves in Fig. 10) (according to the estimated posterior distributions) indicate that the BR model exhibits a better concentration around the true value. To further evaluate the uncertainties, Fig. 11a–c shows the results of one hundred samplings in detail and the estimated posterior distributions (for example, at the spatial point of 2.46 s). The posterior distributions are estimated by assuming the Gaussian
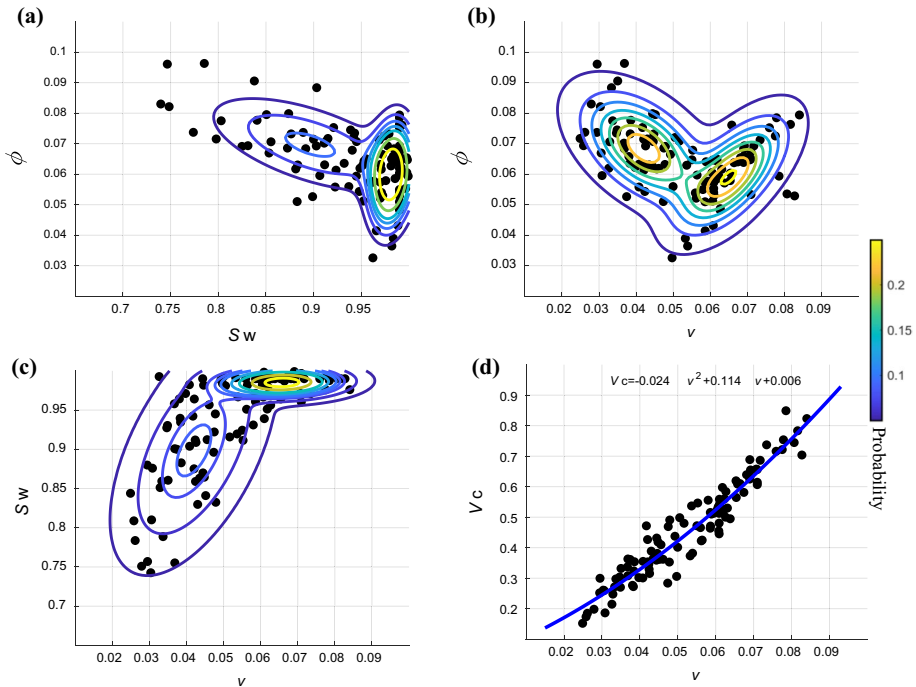
Fig. 7 Gaussian mixture distribution of **a** porosity and saturation, **b** porosity and inclusion volume, **c** saturation and inclusion volume, estimated from the log samples of Well 1, and **d** empirical relationship between the clay and inclusion volume. The inclusion volume is estimated from the well calibration as shown in Fig. 6c

mixture model with three (Gaussian) components, of which statistical parameters are computed by using the expectation–maximization algorithm. Figure 11d–f displays an overall comparison among the posterior distributions, overlain by the relevant prior distributions, from which we can see that the porosity predicted by the proposed method (red curve in Fig. 11d) exhibits the best accuracy with the least uncertainty (the narrowest distribution tail). Although the saturation estimated by the single misfit method (blue curve in Fig. 11e) exhibits a slightly better accuracy than that of the proposed method (red curve), the latter shows a narrower distribution with fewer uncertainties. The clay volume estimated by the proposed method (red curve in Fig. 11f) shows a better accuracy than the others. However, all the methods overestimate the clay content.

3.3 Field data application

We apply the methodology to invert a seismic section (Fig. 12), penetrated by Well 2 at the 83rd common depth point (CDP), where the gas layer of interest is identified between 2.50 and 2.54 s (with a depth of ~ 4.5 km). The section has 146 CDPs, and each CDP contains 6 angle traces ranging from 5 to 30 degrees. In order to validate the method by a blind test, we exclude Well 2 from formulating the prior term and only make use of the data samples of Well 1. The target gas layer in Well 2 has a relatively lower water saturation of 0.6–0.7 (compared with 0.8 in Well 1), and we set the mean
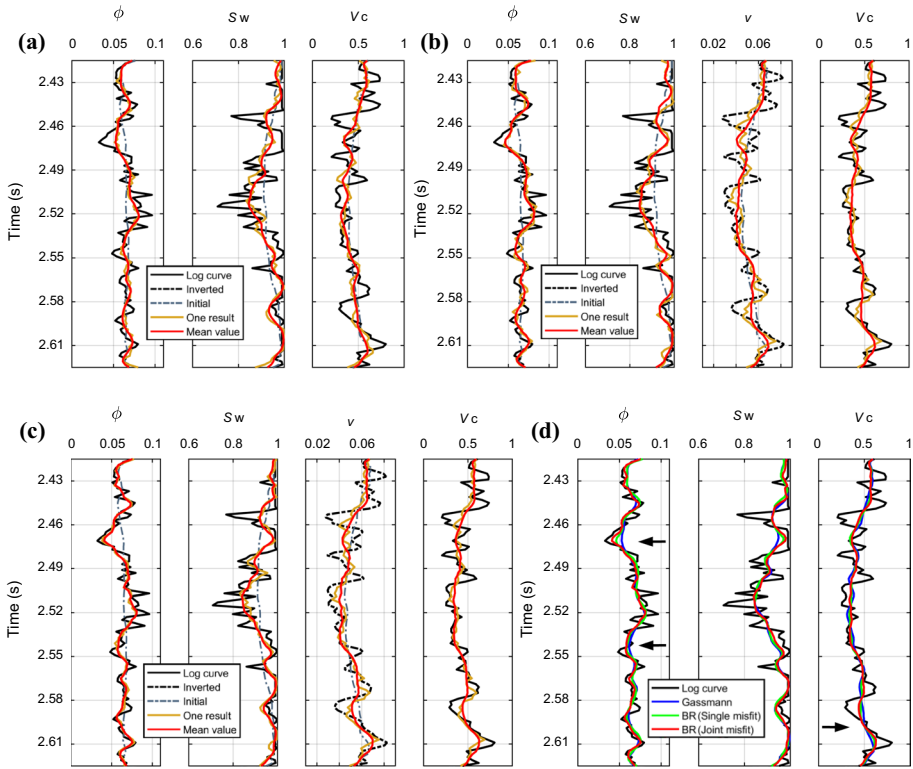
Fig. 8 Inversion results by using **a** the DEM-Gassmann model, **b** the BR model, and **c** the multi-objective BR method (the proposed method), and **d** mean results in the respective plots (**a–c**), where the arrows indicate the improvements achieved by the proposed method

Table 2 Correlation coefficients between the log data and the mean results in Fig. 8d

	ϕ	S_w	V_c
Gassmann model	0.738	0.776	0.609
BR model with a single misfit	0.768	0.796	0.628
BR model with joint misfits	0.821	0.795	0.634

value of saturation to 0.68 for the Gaussian component of the reservoir rocks. The field data inversion is performed trace by trace; hence, the initial temperature of the fast simulated annealing (FSA) varies in different traces, and it is estimated by setting the initial acceptance probability to 90% (other settings are the same as those of the well-log data test).

Figure 13 shows the P-wave velocity model from prestack AVO inversion. The inverted model has a correlation coefficient of 0.81 with the log curve and is used as input elastic data to measure the elastic misfit. The initial values of the posterior weights are set to 0.0015 and 0.023 according to the data variances. Figures 14 and 15 show the inversion results by using the Gassmann and proposed methods, respectively.
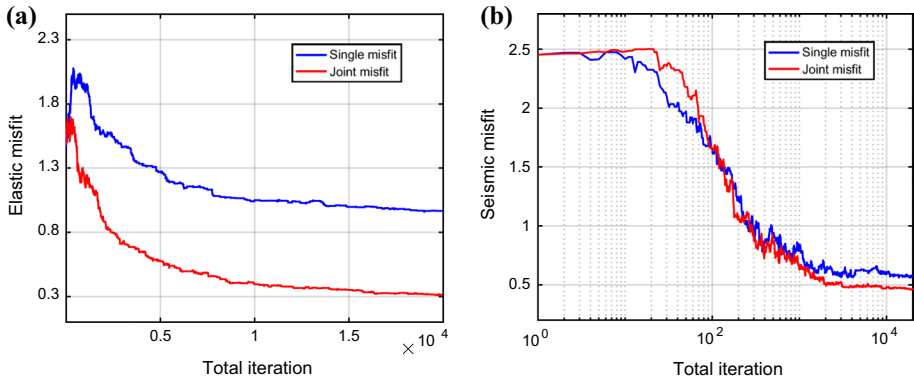
Fig. 9 Evolution for **a** elastic and **b** seismic misfits by the BR model with a single misfit (Fig. 8b) and **b** joint misfits (Fig. 8c)
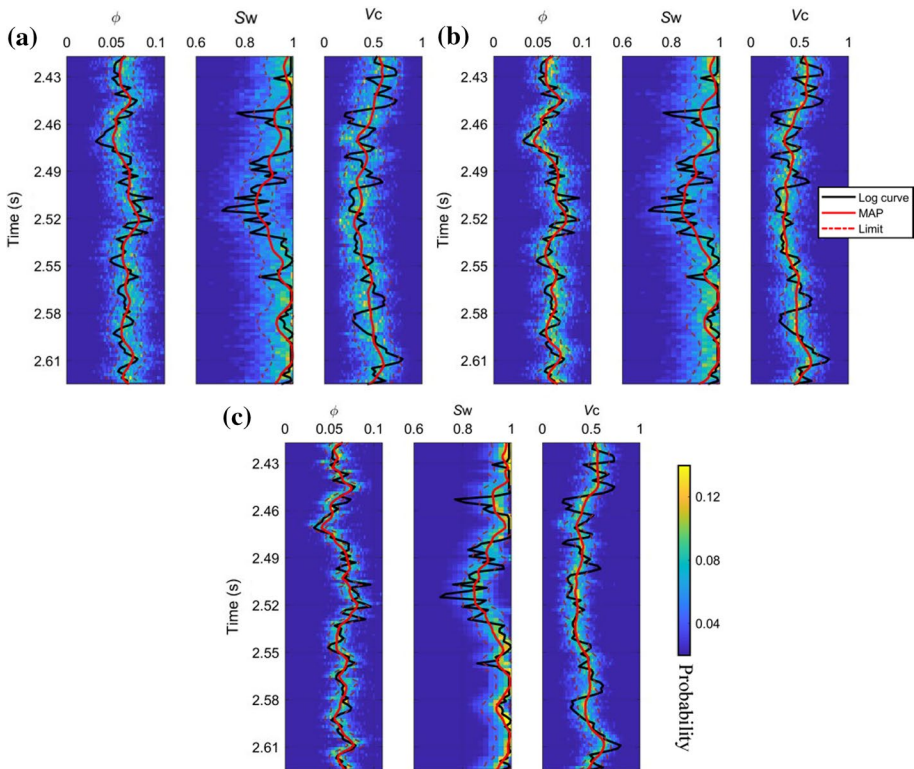

Fig. 10 Posterior distribution by using **a** the Gassmann model, **b** BR model with a single misfit, and **c** multi-objective BR model with joint misfits (the proposed method), overlapped by the MAP estimation (solid red) and 90% confidence limit (dashed red)
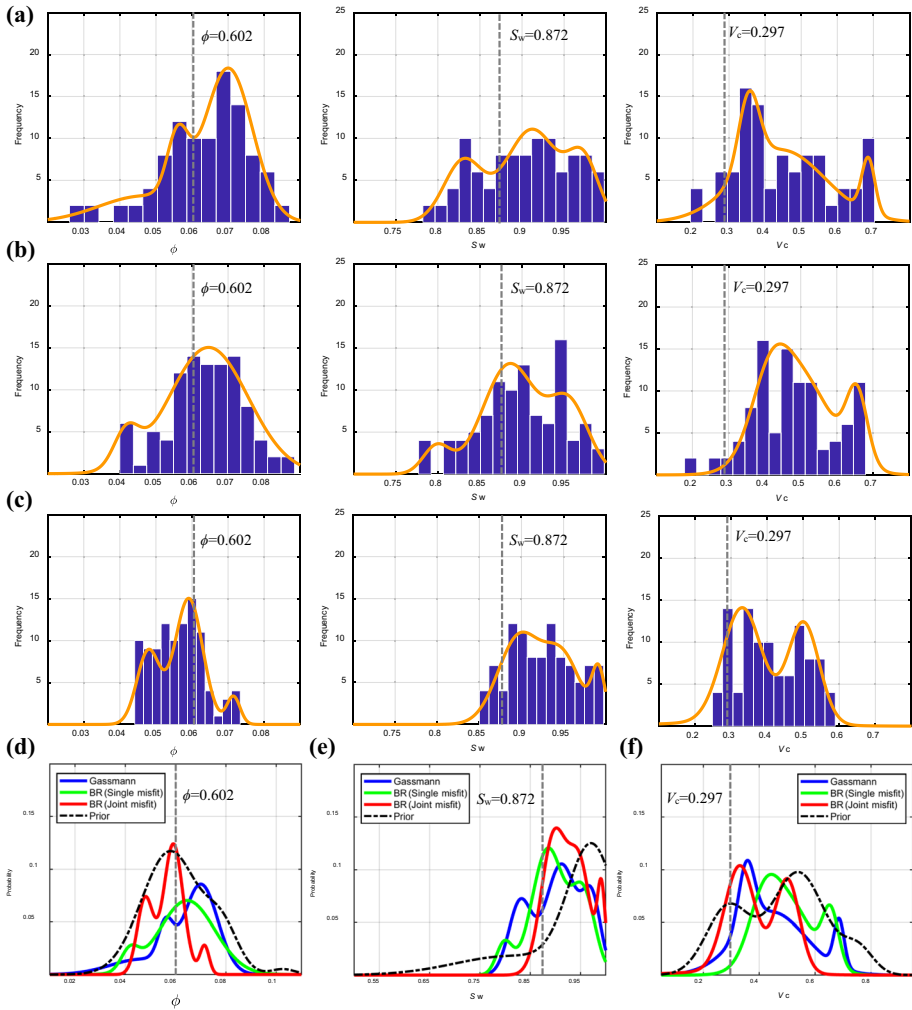
Fig. 11 Histogram of one hundred sampling results at depth of 2.46 s by using **a** Gassmann model, **b** BR model with a single misfit, and **c** the multi-objective BR model with joint misfits, and overall comparison between the posterior distributions (estimated from the sampling results) and the prior distributions for **d** porosity, **e** water saturation, and **f** clay volume. The gray dash lines indicate the true values

The porosity predicted by the BR model (Fig. 15a) exhibits a better performance to identify the reservoir rocks, where the prediction fairly agrees with the log profiles. In contrast, the Gassmann method (Fig. 14a) generally underestimates the porosity and also exhibits a poor lateral continuity along the gas layer. Although the accuracy in estimating the water saturation for the gas zone by the two methods is comparable, the BR model (Fig. 15b) removes a few anomalies in the non-reservoir areas. The clay volume (Fig. 15c) predicted by this model is obtained from the inverted inclusion volume. Since the conversion highly depends on the in-situ fit (empirical) relation, no apparent
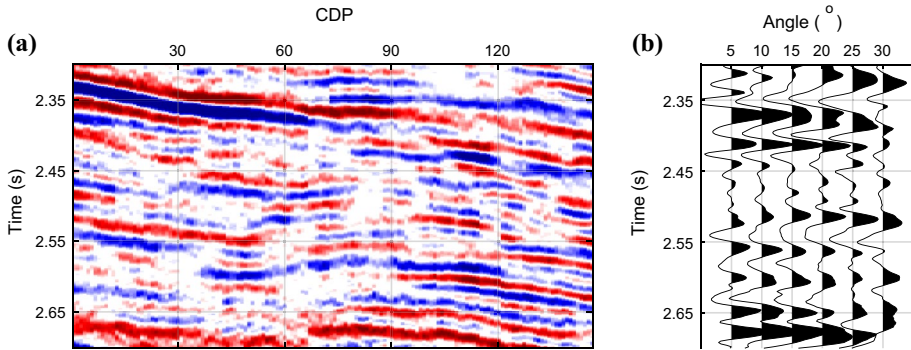
Fig. 12 **a** Stacked section and **b** angle gather at the 100th CDP

Fig. 13 P-wave velocity model from prestack AVO inversion that is used as input data to formulate the elastic misfit term of the objective function
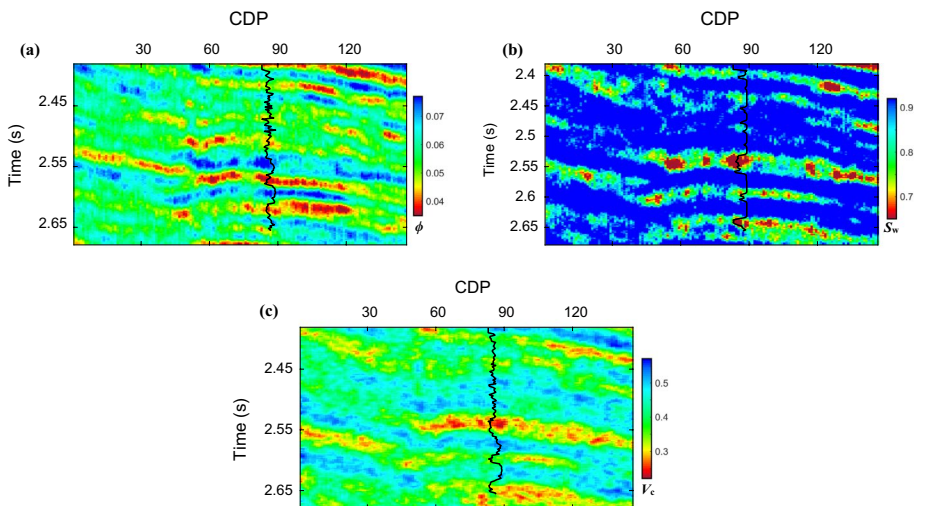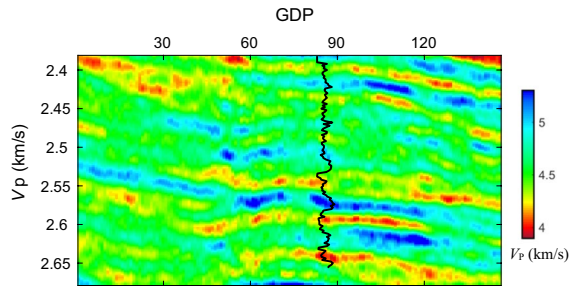

Fig. 14 Inversion of **a** porosity, **b** water saturation, and **c** clay volume by the Gassmann model, overlaid by the log curve of Well 2
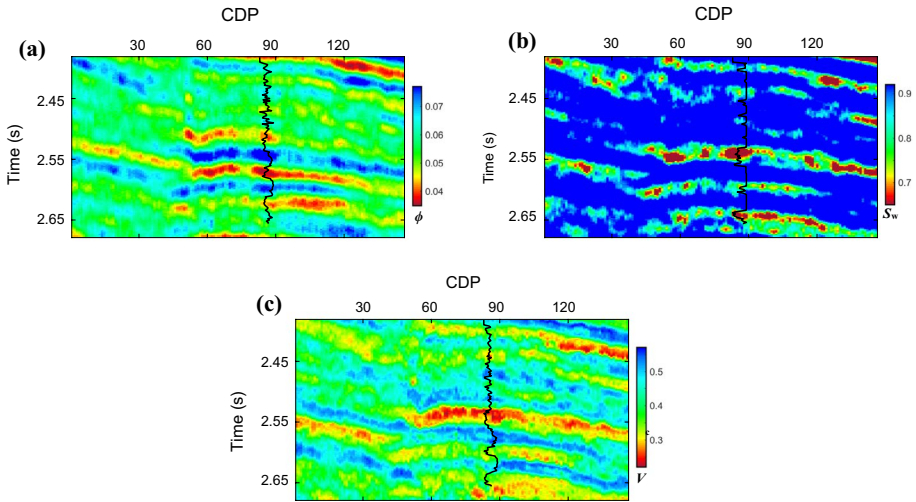
Fig. 15 Inversion of **a** porosity, **b** water saturation, and **c** inclusion volume by the proposed BR model, overlaid by the log curve of Well 2
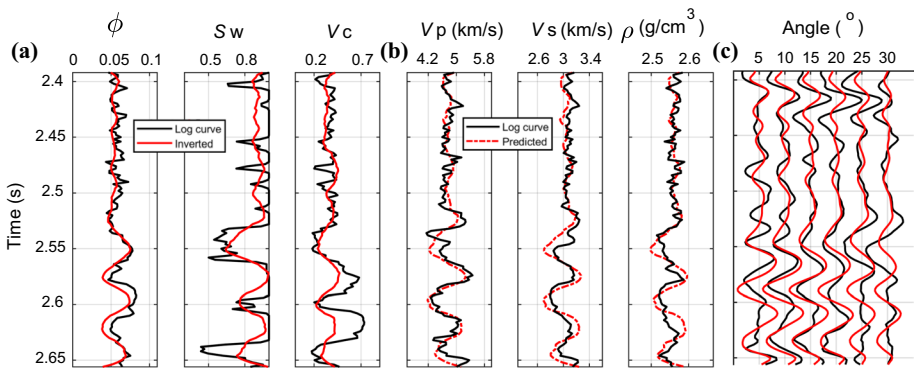

Fig. 16 Blind test on Well 2 for **a** inverted petrophysical parameters (solid red) and **b** predicted elastic parameters (dashed red), and **c** comparison between the predicted and observed angle gathers at the 83rd CDP

improvement is observed in this case. Nevertheless, the clay-volume estimation is useful to identify the zones with relatively lower clay content, which may be helpful to delineate the gas zones.

Furthermore, Fig. 16 displays the result (red curve) by the proposed BR method, compared with the log data (black curve). Generally, the agreement for the petrophysical parameters is acceptable and the porosity exhibits a fairly good match. The correlation coefficients with the log curves (blind test) are 0.736, 0.693, and 0.612, for the porosity, saturation, and clay-volume results, respectively. The predicted elastic parameters (from the inverted petrophysical parameters in Fig. 16a) generally honor the log profiles (Fig. 16b), and the predicted seismic data also show an acceptable agreement

with the borehole-side angle gather (Fig. 16c). However, the clay volume (converted from the inclusion volume) underestimates the result to some degree, probably due to uncertainties in the derived empirical relation by excluding the data of Well 2.

3.4 Discussion

The proposed method is applied to a tight gas sandstone reservoir in this paper, and it can be extended to other reservoirs (e.g., carbonates) by considering the capability of the BR model to describe heterogeneous rocks (Ba et al. 2017; Pang et al. 2020), but a different approach to obtain the elastic properties of the host/inclusion skeletons may be required. Here, we have used this model at seismic frequencies (~ 50 Hz), although it is more general. The inclusion of frequency-dependent properties, such as seismic attenuation and dispersion, may improve the inversion and will be a task for future work. The method combines the joint (single-step) and sequential inversion approaches in which the estimation is conditioned both to seismic and elastic data. The well-log data test demonstrates that, provided the input P-wave velocity data having a coefficient correlation of 0.85 with the log curve, the method can be better than the joint approach (being conditioned only to seismic data). The elastic data with low quality may cause deviations in the elastic misfit term of objective function and thereby worsen the convergence performance of optimization process, which will affect the prediction of reservoir parameters. Besides, we only set P-wave velocity as the input elastic data, whereas including S-wave velocity or bulk density as an additional input may facilitate improving the result but would cause more uncertainties associated with the elastic data accuracy and acquisition. We solve the problem by minimizing a linear weighted objective function by a global optimization algorithm while updating the weights via stochastic sampling estimation. However, other optimizations or sampling methods, e.g., Pareto optimization (Zidan et al. 2021), can be applied to have comparable or even better performance. One drawback is that for inverting a seismic section, the BR method consumes more than twice computer time than the Gassmann model, which takes 8.5 h on a standard workstation. Therefore, the efficiency should be improved when the method is applied to 3D seismic data.

4 Conclusions

We have proposed a seismic petrophysical inversion method by combining the DEM and double-porosity Biot–Rayleigh models with the Zoeppritz equation, to extract reservoir properties. The inversion method takes into account the rock microstructure, yielding better results than Gassmann-based methods under complex reservoir conditions. The inclusion volumes in the Biot–Rayleigh equation are unknown variables to account for the heterogeneities and handle spatially complex structures. The estimation of the petrophysical properties is formulated as a multi-objective optimization problem, where the objective function contains joint data misfits and multiple prior terms, to stabilize the algorithm with reduced uncertainties. The method is successfully validated by tests on data from a tight gas sandstone reservoir.

Appendix A: The Biot–Rayleigh equation and its plane-wave solution

Ba et al. (2011) proposed the Biot–Rayleigh model to describe the seismic wave propagation in a double-porosity medium. The governing equations are

$$N\nabla^2\mathbf{u} + (A + N)\nabla\varepsilon + Q_1(\zeta^{(1)} + \phi_c\varsigma) + Q_2(\zeta^{(2)} - \phi_1\varsigma)$$
$$= \rho_{11}\ddot{\mathbf{u}} + \rho_{12}\ddot{\mathbf{U}}^{(1)} + \rho_{13}\ddot{\mathbf{U}}^{(2)} + b_1(\dot{\mathbf{u}} - \dot{\mathbf{U}}^{(1)}) + b_2(\dot{\mathbf{u}} - \dot{\mathbf{U}}^{(2)}), \tag{19}$$

$$Q_1\nabla\varepsilon + R_1\nabla(\zeta^{(1)} + \phi_c\varsigma) = \rho_{12}\ddot{\mathbf{u}} + \rho_{22}\ddot{\mathbf{U}}^{(1)} - b_1(\dot{\mathbf{u}} - \dot{\mathbf{U}}^{(1)}), \tag{20}$$

$$Q_2\nabla\varepsilon + R_2\nabla(\zeta^{(2)} - \phi_1\varsigma) = \rho_{13}\ddot{\mathbf{u}} + \rho_{33}\ddot{\mathbf{U}}^{(1)} - b_2(\dot{\mathbf{u}} - \dot{\mathbf{U}}^{(2)}), \tag{21}$$

$$\phi_c(Q_1\varepsilon + R_1(\zeta^{(1)} + \phi_c\varsigma)) - \phi_1(Q_2\varepsilon + R_2(\zeta^{(2)} - \phi_1\varsigma))$$
$$= \frac{1}{3}\rho_f\ddot{\varsigma}R_0^2\frac{\phi_1^2\phi_2\phi_{20}}{\phi_{10}} + \frac{1}{3}\frac{\eta\phi_1^2\phi_2\phi_{20}}{\kappa_1}\dot{\varsigma}R_0^2, \tag{22}$$

where $\mathbf{u}$, $\mathbf{U}^{(1)}$, and $\mathbf{U}^{(2)}$ are the average particle displacements of the skeleton, and the average fluid displacements in the host and inclusion, respectively, with volume strains ε, $\zeta^{(1)}$, and $\zeta^{(2)}$, ϕ_{10} and ϕ_{20} are the porosities of the host and inclusion with their absolute porosities ϕ_1 and ϕ_2, κ_1 and η are the host-medium permeability and fluid viscosity, respectively, ς denotes the fluid strain increment in the local fluid flow and R_o is the radius of inclusion. The equations contain six stiffness parameters A, N, Q_1, Q_2, R_1, R_2, five density coefficients $\rho_{11}, \rho_{12}, \rho_{13}, \rho_{22}, \rho_{33}$, and two Biot dissipation coefficients b_1 and b_2.

By substituting a plane-wave kernel into Eqs. (19)–(20), the complex wave number k can be obtained from

$$\begin{vmatrix} a_{11}k^2 + b_{11} & a_{12}k^2 + b_{12} & a_{13}k^2 + b_{13} \\ a_{21}k^2 + b_{21} & a_{22}k^2 + b_{22} & a_{23}k^2 + b_{23} \\ a_{31}k^2 + b_{31} & a_{32}k^2 + b_{32} & a_{33}k^2 + b_{33} \end{vmatrix} = 0, \tag{23}$$

where

$$\begin{aligned}
a_{11} &= A + 2N + i(Q_2\phi_1 - Q_1\phi_2)x_1, \\
b_{11} &= -\rho_{11}\omega^2 + i\omega(b_1 + b_2), \\
a_{12} &= Q_1 + i(Q_2\phi_1 - Q_1\phi_2)x_2, \ b_{12} = -\rho_{12}\omega^2 - i\omega b_1, \\
a_{13} &= Q_2 + i(Q_2\phi_1 - Q_1\phi_2)x_3, \ b_{13} = -\rho_{13}\omega^2 - i\omega b_2, \\
a_{21} &= Q_1 - iR_1\phi_2 x_3, \ b_{21} = -\rho_{12}\omega^2 - i\omega b_1, \\
a_{22} &= R_1 - iR_1\phi_2 x_2, \ b_{22} = -\rho_{22}\omega^2 + i\omega b_1, \\
a_{23} &= -iR_1\phi_2 x_3, \ b_{23} = 0, \\
a_{31} &= Q_2 + iR_2\phi_1 x_1, \ b_{31} = -\rho_{13}\omega^2 - i\omega b_2, \\
a_{32} &= iR_2\phi_1 x_2, \ b_{32} = 0, \\
a_{33} &= R_2 + iR_2\phi_1 x_3, \ b_{33} = -\rho_{33}\omega^2 + i\omega b_2.
\end{aligned} \tag{24}$$

and

$$x_1 = \frac{i(\phi_2 Q_1 - \phi_1 Q_2)}{Z}, \; x_2 = \frac{i\phi_2 R_1}{Z}, \; x_3 = -\frac{i\phi_1 R_2}{Z},$$

$$Z = \frac{i\omega\eta\phi_1^2\phi_2\phi_{20}R_0^2}{3\kappa_1} - \frac{\rho_f\omega^2 R_0^2\phi_1^2\phi_2\phi_{20}}{3\phi_{10}} - (\phi_2^2 R_1 + \phi_1^2 R_2). \tag{25}$$

Equation (23) yields three roots, and we choose the fast P-wave one (the classical compressional wave). The phase velocity is given by Carcione (2014) as

$$V_P = \left[\text{Re}\left(\frac{k}{\omega}\right)\right]^{-1}, \tag{26}$$

where ω is the angular frequency.

Appendix B: Update of posterior weights

Jalobeanu et al. (2002) and Guo et al. (2021a) proposed to update the regularization parameters by using the Monte-Carlo-based maximum likelihood method. We hereby extend the method to be applicable to the multi-objective optimization problem with joint data misfits.

The likelihood function of Eq. (15) is

$$P(\mathbf{d}_{\text{seis}}, \mathbf{d}_{\text{elas}} | \boldsymbol{\beta}) = \sum_{\mathbf{z} \in \Omega} P(\mathbf{d}_{\text{seis}}, \mathbf{d}_{\text{elas}} | \mathbf{z}, \boldsymbol{\beta}) \times P(\mathbf{z} | \boldsymbol{\beta}), \tag{27}$$

where the Ω denotes the data space of $\mathbf{z}$. Given the known $\boldsymbol{\beta}$, we have

$$P(\mathbf{d}_{\text{seis}}, \mathbf{d}_{\text{elas}} | \mathbf{z}, \boldsymbol{\beta}) = P(\mathbf{d}_{\text{seis}}, \mathbf{d}_{\text{elas}} | \mathbf{z}) \approx P(\mathbf{d}_{\text{seis}} | \mathbf{z}) \times P(\mathbf{d}_{\text{elas}} | \mathbf{z}, \boldsymbol{\beta})$$

$$= \frac{1}{K_s} \exp\left(F_1(\mathbf{d}_{\text{seis}}, \mathbf{z})\right) \times \frac{1}{K_e} \exp\left(F_2(\mathbf{d}_{\text{elas}}, \mathbf{z}, \beta_1)\right), \tag{28}$$

where F_1 and F_2 denote the seismic and elastic misfit terms in Eq. (12), and

$$K_s = \sum_{\mathbf{z} \in \Omega} P(\mathbf{d}_{\text{seis}} | \mathbf{z}) \text{ and } K_e = \sum_{\mathbf{z} \in \Omega} P(\mathbf{d}_{\text{elas}} | \mathbf{z}, \beta_1) \tag{29}$$

are the normalization constants.

The prior distribution of $P(\mathbf{z} | \boldsymbol{\beta})$ is

$$P(\mathbf{z} | \boldsymbol{\beta}) = \frac{1}{K_\beta} \exp\left(F_3(\mathbf{z}, \beta_2)\right), \tag{30}$$

where F_3 denotes the prior term in Eq. (12), and

$$K_\beta = \sum_{\mathbf{z} \in \Omega} \exp\left(F_3(\mathbf{z}, \beta_2)\right) \tag{31}$$

is a normalization constant.

By substituting Eqs. (28) and (30) into (27), the likelihood function of $\boldsymbol{\beta}$ can be expressed as the negative logarithm of $P(\mathbf{d}_{\text{seis}}, \mathbf{d}_{\text{elas}} | \boldsymbol{\beta})$

$$L(\boldsymbol{\beta}) = -\ln\left(\frac{K_z}{K_s K_e K_\beta}\right) = \ln K_z - \ln K_s - \ln K_e - \ln K_\beta, \tag{32}$$

with

$$K_z = \sum_{\mathbf{z}\in\Omega} \exp\left(F_1\left(\mathbf{d}_{\text{seis}}, \mathbf{z}\right) \ F_2\left(\mathbf{d}_{\text{elas}}, \mathbf{z}, \beta_1\right) F_3\left(\mathbf{z}, \beta_2\right)\right). \tag{33}$$

By employing the Gauss–Newton descent method to minimize the log-likelihood function 32, $\boldsymbol{\beta}$ can be iteratively updated as

$$\boldsymbol{\beta}^{(n+1)} = \boldsymbol{\beta}^{(n)} - \left[\left(\frac{\partial L}{\partial \boldsymbol{\beta}}\right)^{\mathrm{T}}\left(\frac{\partial L}{\partial \boldsymbol{\beta}}\right)\right]\frac{\partial L}{\partial \boldsymbol{\beta}}, \tag{34}$$

with

$$\begin{aligned}
\frac{\partial L}{\partial \boldsymbol{\beta}} &= \sum_{\mathbf{z}\in\Omega}\left(-\frac{\partial F_2}{\partial \boldsymbol{\beta}} - \frac{\partial F_3}{\partial \boldsymbol{\beta}}\right)\frac{1}{K_z}\exp\left(F_1 \ F_2 \ F_3\right) \\
&\quad - \sum_{\mathbf{z}\in\Omega}\left(-\frac{\partial F_2}{\partial \boldsymbol{\beta}}\right)\frac{1}{K_e}\exp\left(F_2\right) - \sum_{\mathbf{z}\in\Omega}\left(-\frac{\partial F_3}{\partial \boldsymbol{\beta}}\right)\frac{1}{K_\beta}\exp\left(F_3\right).
\end{aligned} \tag{35}$$

Introducing the expectation of $\mathbf{z}$, regarding its probability distribution, Eq. (35) can be estimated from the expectations of one prior distribution (E_β) and two posterior distributions (E_z and E_e) as

$$\frac{\partial L}{\partial \boldsymbol{\beta}} = -E_z\left(\frac{\partial F_2}{\partial \boldsymbol{\beta}}\right) - E_z\left(\frac{\partial F_3}{\partial \boldsymbol{\beta}}\right) + E_e\left(\frac{\partial F_2}{\partial \boldsymbol{\beta}}\right) + E_\beta\left(\frac{\partial F_3}{\partial \boldsymbol{\beta}}\right). \tag{36}$$

By setting the quadratic form of $\boldsymbol{\beta} = \left[\beta_1^2, \beta_2^2\right]^{\mathrm{T}}$ to compute the derivative and to ensure its value positive, the derivative in Eq. (32) [or Eq. (16)] can be estimated as

$$\frac{\partial L}{\partial \boldsymbol{\beta}} = \begin{pmatrix} \dfrac{\partial L}{\partial \beta_1} \\[2mm] \dfrac{\partial L}{\partial \beta_2} \end{pmatrix} = \begin{pmatrix} -2\beta_1\left(E_z\left(F_2^*\right) - E_e\left(F_2^*\right)\right) \\ -2\beta_2\left(E_z\left(F_3^*\right) - E_\beta\left(F_3^*\right)\right) \end{pmatrix}, \tag{37}$$

where $F_2^{\ *}$ and $F_3^{\ *}$ denote the F_2 and F_3 terms without β_1 and β_2.

References

Aki K, Richards PG (1980) Quantitative seismology. W H Freeman & Co

Aleardi M, Ciabarri F, Calabrò R (2018) Two-stage and single-stage seismic-petrophysical inversions applied in the Nile Delta. Lead Edge 37(7):510–518

Astic T, Heagy LJ, Oldenburg DW (2021) Petrophysically and geologically guided multi-physics inversion using a dynamic Gaussian mixture model. Geophys J Int 224(1):40–68

Avseth P, Bachrach R (2005) Seismic properties of unconsolidated sands: tangential stiffness, Vp/Vs ratios and diagenesis. In: SEG Technical Program Expanded Abstracts, pp 1473–1476

Avseth P, Veggeland T (2014) Seismic screening of rock stiffness and fluid softening using rock-physics attributes. Interpretation 3(4):SAE85–SAE93

Azevedo L, Grana D, Amaro C (2019) Geostatistical rock physics AVA inversion. Geophys J Int 216(3):1728–1739

Bachrach R (2006) Joint estimation of porosity and saturation using stochastic rock-physics modeling. Geophysics 71(5):O53–O63

Ba J, Carcione JM, Nie J (2011) Biot-Rayleigh theory of wave propagation in double-porosity media. J Geophys Res 116:B06202

Ba J, Xu W, Fu L-Y, Carcione JM, Zhang L (2017) Rock anelasticity due to patchy-saturation and fabric heterogeneity: a double double-porosity model of wave propagation. J Geophys Res 122:1949–1971

Berryman JG, Pride SR, Wang HF (2002) A differential scheme for elastic properties of rocks with dry or saturated cracks. Geophys J Int 151:597–611

Bosch M, Cara L, Rodrigues J, Navarro A, Díaz M (2007) A Monte Carlo approach to the joint estimation of reservoir and elastic parameters from seismic amplitudes. Geophysics 72(6):O29–O39

Bosch M, Mukerji T, Gonzalez EF (2010) Seismic inversion for reservoir properties combining statistical rock physics and geostatistics: a review. Geophysics 75(5):75A165-75A176

Bredesen K, Rasmussen R, Mathiesen A, Nielsen LH (2021) Seismic amplitude analysis and rock physics modeling of a geothermal sandstone reservoir in the southern part of the Danish Basin. Geothermics 89:101974

Buland A, Omre H (2003) Bayesian linearized AVO inversion. Geophysics 68(1):185–198

Carcione JM, Gurevich B, Santos JE, Picotti S (2013) Angular and frequency dependent wave velocity and attenuation in fractured porous media. Pure Appl Geophys 170:1673–1683

Carcione JM (2014) Wavefields in real media: Theory and numerical simulation of wave propagation in anisotropic, anelastic, porous and electromagnetic media, 3rd edn. Elsevier

Chen H, Moradi S, Innanen KA (2021) Joint inversion of frequency components of PP- and PSV-wave amplitudes for attenuation factors using second-order derivatives of anelastic impedance. Surv Geophys 42:961–987

Connolly PA, Hughes MJ (2016) Stochastic inversion by matching to large numbers of pseudo-wells. Geophysics 81(2):M7–M22

David EC, Zimmerman RW (2012) Pore structure model for elastic wave velocities in fluid-saturated sandstones. J Geophys Res 117:B07210

de Figueiredo LP, Grana D, Roisenberg M, Rodrigues BB (2019) Multimodal Markov chain Monte Carlo method for nonlinear petrophysical seismic inversion. Geophysics 84(5):M1–M13

Dvorkin J, Gutierrez M, Grana D (2014) Seismic reflections of rock properties. Cambridge University Press

Dvorkin J, Nur A (1993) Dynamic poroelasticity: a unified model with the squirt and the Biot mechanisms. Geophysics 58(4):524–533

Fjeldstad T, Avseth P, Omre H (2021) A one-step Bayesian inversion framework for 3D reservoir characterization based on a Gaussian mixture model: a Norwegian Sea demonstration. Geophysics 86(2):R221–R236

Gassmann F (1951) Elastic waves through a packing of spheres. Geophysics 16(4):673–685

González EF, Mukerji T, Markov G (2008) Seismic inversion combining rock physics and multiple-point geostatistics. Geophysics 73(1):R11–R21

Grana D, Fjeldstad T, Omre H (2017) Bayesian Gaussian mixture linear inversion for geophysical inverse problems. Math Geosci 49:493–515

Grana D (2020) Bayesian petroelastic inversion with multiple prior models. Geophysics 85(5):M57–M71

Gunning J, Glinsky M (2007) Detection of reservoir quality using Bayesian seismic inversion. Geophysics 72(3):R37–R49

Gurevich B, Brajanovski M, Galvin RJ, Muller TM, Toms-Stewart J (2009) P-wave dispersion and attenuation in fractured and porous reservoirs: poroelasticity approach. Geophys Prospect 57(2):225–237

Guo Q, Ba J, Fu L-Y, Luo C (2021a) Joint seismic and petrophysical nonlinear inversion with Gaussian mixture-based adaptive regularization. Geophysics 86(6):R895–R911

Guo Q, Ba J, Luo C, Pang M (2021b) Seismic rock physics inversion with varying pore aspect ratio in tight sandstone reservoirs. J Petrol Sci Eng 207:109131

Hafez A, Majoor F, Castagna JP (2014) Deepwater reservoir heterogeneity delineation using rock physics and extended elastic impedance inversion: Nile Delta case study. Interpretation 2(4):T205–T219

Hammer H, Kolbjørnsen O, Tjelmeland H, Buland A (2012) lithofacies and fluid prediction from prestack seismic data using a Bayesian model with Markov process prior. Geophys Prospect 60(3):500–515

Hansen TM, Journel AG, Tarantola A, Mosegaard K (2006) Linear inverse Gaussian theory and geo-statistics. Geophysics 71(6):R101–R111

Huang G, Chen X, Luo C, Chen Y (2021a) Mesoscopic wave-induced fluid flow effect extraction by using frequency-dependent prestack waveform inversion. IEEE Trans Geosci Remote Sens 59(8):6510–6524

Huang G, Chen X, Li J, Saad OM, Fomel S, Luo C, Wang H, Cheng Y (2021b) The slope-attribute-regularized high-resolution prestack seismic inversion. Surv Geophys 42:625–671

Ingber L, Rosen B (1992) Genetic algorithms and very fast simulated reannealing: a comparison. Math Comput Model 16:87–100

Jalobeanu A, Blanc-Feraud L, Zerubia J (2002) Hyperparameter estimation for satellite image restoration using a MCMC maximum likelihood method. Pattern Recogn 35(2):341–352

Li K, Yin X, Zong Z, Lin H (2021) Direct estimation of discrete fluid facies and fluid indicators via a Bayesian seismic probabilistic inversion and a novel exact PP-wave reflection coefficient. J Petrol Sci Eng 196:107412

Luo C, Ba J, Carcione J, Huang G, Guo Q (2020) Joint PP and PS pre-stack seismic inversion for stratified models based on the propagator matrix forward engine. Surv Geophys 41:987–1028

Markov M, Levine V, Mousatov A, Kazatchenko E (2005) Elastic properties of double-porosity rocks using the differential effective medium model. Geophys Prospect 53(5):733–754

Mavko G, Mukerji T, Dvorkin J (2009) The rock physics handbook: tools for seismic analysis of porous media. Cambridge University Press

Mosegaard K (1998) Resolution analysis of general inverse problems through inverse Monte Carlo sampling. Inverse Prob 14:405–426

Norris AN (1985) A differential scheme for the effective moduli of composites. Mech Mater 4(1):1–16

Pan X, Zhang G (2018) Model parameterization and PP-wave amplitude versus angle and azimuth (AVAZ) direct inversion for fracture quasi-weaknesses in weakly anisotropic elastic media. Surv Geophys 39:937–964

Pang M, Ba J, Fu L-Y, Carcione JM, Markus UI, Zhang L (2020) Estimation of microfracture porosity in deep carbonate reservoirs based on 3D rock-physics templates. Interpretation 8(4):43–52

Pang M, Ba J, Carcione JM (2021) Characterization of gas saturation in tight-sandstone reservoirs with rock-physics templates based on seismic Q. J Energ Eng 147(3):04021011

Pride SR, Berryman JG, Harris JM (2004) Seismic attenuation due to wave-induced flow. J Geophys Res 109:B01201

Picotti S, Carcione JM, Ba J (2018) Rock-physics templates for seismic Q. Geophysics 84(1):MR13–MR23

Ryden N, Park CB (2006) Fast simulated annealing inversion of surface waves on pavement using phase-velocity spectra. Geophysics 71(4):R49–R58

Sambridge M, Mosegaard K (2002) Monte Carlo methods in geophysical inverse problems. Rev Geophys 40(3):1–29

Santos JE, Ravazzoli CL, Carcione JM (2004) A model for wave propagation in a composite solid matrix saturated by a single-phase fluid. J Acoust Soc Am 115:2749–2760

Sauvageau M, Gloaguen E, Claprood M, Lefebvre R, Bêche M (2014) Multimodal reservoir porosity simulation: an application to a tight oil reservoir. J Appl Geophys 107:71–79

Sen MK, Stoffa PL (2013) Global optimization methods in geophysical inversion. Cambridge University Press

Spikes K, Mukerji T, Dvorkin J, Mavko G (2007) Probabilistic seismic inversion based on rock- physics models. Geophysics 72(5):R87–R97

Teillet T, Fournier F, Zhao L, Borgomano J, Hong F (2021) Geophysical pore type inversion in carbonate reservoir: integration of cores, well logs, and seismic data (Yadana field, offshore Myanmar). Geophysics 86(3):B149–B164

Wang E, Carcione JM, Ba J, Liu Y (2020) Reflection and transmission of plane elastic waves at an interface between two double-porosity media: effect of local fluid flow. Surv Geophys 41:283–322

Wang H, Tang X (2021) Inversion of dry and saturated P- and S-wave velocities for the pore-aspect-ratio spectrum using a cracked porous medium elastic wave theory. Geophysics 86(6):A57–A62

Wang P, Chen X, Li X, Cui Y, Li J, Wang B (2021) Analysis and estimation of an inclusion-based effective fluid modulus for tight gas-bearing sandstone reservoirs. IEEE Trans Geosci Remote Sens (online). https://doi.org/10.1109/TGRS.2021.3099134

Xu S, White RE (1995) A new velocity model for clay-sand mixtures. Geophys Prospect 43:91–118

Yan J, Li X, Liu E (2002) Effects of pore aspect ratios on velocity prediction from well-log data. Geophys Prospect 50(3):289–300

Zhao L, Nasser M, Han DH (2013) Quantitative geophysical pore type characterization and its geological implication in carbonate reservoirs. Geophys Prospect 61(4):827–841

Zong Z, Yin X, Wu G (2015) Geofluid discrimination incorporating poroelasticity and seismic reflection inversion. Surv Geophys 36:659–681

Zidan A, Li YE, Cheng A (2021) A Pareto multi-objective optimization approach for anisotropic shale models. J Geophys Res 126:e2020JB021476

Publisher's Note Springer Nature remains neutral with regard to jurisdictional claims in published maps and institutional affiliations.